

A minimal model for structure, dynamics, and tension of monolayered cell colonies

Debarati Sarkar,^{1,*} Gerhard Gompper,^{1,†} and Jens Elgeti^{1,‡}

¹*Theoretical Physics of Living Matter, Institute of Biological Information Processing and Institute for Advanced Simulation, Forschungszentrum Jülich, D-52425 Jülich, Germany*

The motion of cells in tissues is an ubiquitous phenomenon. In particular, in monolayered cell colonies *in vitro*, pronounced collective behavior with swirl-like motion has been observed deep within a cell colony, while at the same time, the colony remains cohesive, with not a single cell escaping at the edge. Thus, the colony displays liquid-like properties inside, in coexistence with a cell-free “vacuum” outside. How can adhesion be strong enough to keep cells together, while at the same time not jam the system in a glassy state? What kind of minimal model can describe such a behavior? Which other signatures of activity arise from the internal fluidity? We propose a novel active Brownian particle model with attraction, in which the interaction potential has a broad minimum to give particles enough wiggling space to be collectively in the fluid state. We demonstrate that for moderate propulsion, this model can generate the fluid-vacuum coexistence described above. In addition, the combination of the fluid nature of the colony with cohesion leads to preferred orientation of the cell polarity, pointing outward, at the edge, which in turn gives rise to a tensile stress in the colony – as observed experimentally for epithelial sheets. For stronger propulsion, collective detachment of cell clusters is predicted. Further addition of an alignment preference of cell polarity and velocity direction results in enhanced coordinated, swirl-like motion, increased tensile stress and cell-cluster detachment.

Keywords: collective cell migration | liquid-vacuum coexistence | tensile stress | cellular velocity alignment | coordinated motion

I. INTRODUCTION

Many fundamental biological processes, like embryogenesis, wound healing or cancer/tumor invasion require cells to move collectively within tissues [1–3]. The physics underlying these processes ranges from understanding actin polymerization and tread-milling for force generation [4, 5] and single cell migration [6, 7], to the collective behavior of many migrating cells [8–10]. Here, we focus on an observation from monolayers of migrating Madin-Darby canine kidney (MDCK) cells on surfaces, a prototypical model system for collective cell migration. Experimental observations reveal large-scale collective motion, like swirls, within the bulk of young monolayers [11, 12], thus the display of fluid-like properties, before jamming occurs as the epithelial sheet matures [13–16]. Interestingly, as an initial colony expands, no cells detach from the boundary — even though the bulk of the tissue remains clearly fluid-like [9]. Cohesion is strong enough that fingers of many cells can protrude at the propagating tissue front without cell detachment. Even stronger-pulling “leader cells” do not detach [17–20]. Cells are thus in a ‘liquid-vacuum’¹ coexistence regime. Even more surprising, pioneering experiments have revealed that these expanding colonies are under tensile stress [22, 23]. This raises the question how this liquid-vacuum coexistence, in combination with strong

collective motion and tensile stress, can be captured and understood from a minimal physical model.

An active Brownian particle (ABP) model [24–27] for cells with standard attractive Lennard-Jones (LJ) interactions has been proposed to study cell colonies [28–30]. However, only solid-vacuum (no fluidity of the condensed phase), or liquid-gas (finite cell density in the dilute phase) coexistence has been obtained. The coexistence of liquids with a very-low-density gas phase is of course well known in many equilibrium systems. In the biological context, for example, lipid-bilayer membranes are liquid in nature, but the critical-micelle concentration is very low, so that lipids essentially never detach from the membrane. In the modelling and simulation of lipid membranes, a similar problem of attractive interactions and fluidity exists as for cell monolayers – too strong attraction leads to solidification. In coarse-grained simulations of lipid bilayers, this problem was overcome by an interaction potential with an extended range compared with the standard Lennard-Jones potential, which provides strong adhesion while still giving enough wiggle room for the molecules that the membrane to remain the fluid phase [31]. In the spirit of minimal modeling, we propose an active Brownian particle (ABP) model for the cells, combined with a similar longer-range interaction potential as employed successfully for the membrane lipids. We demonstrate that the LJ potential with a wider attractive basin indeed opens up a region in phase space that displays liquid-vacuum coexistence. The size of the liquid-vacuum region expands as the basin width of LJ potential increases. The fluidity of the condensed phase implies the emergence of several interesting behaviors, like a tensile stress within the colony due to a preferred orientation of the boundary cells to the out-

*Electronic address: d.sarkar@fz-juelich.de

†Electronic address: g.gompper@fz-juelich.de

‡Electronic address: j.elgeti@fz-juelich.de

¹ We use the term ‘vacuum’ here somewhat loosely to represent a phase of extremely low cell density

side, as well as the detachment of cell cluster above a size threshold. When a coupling of cell polarity to the instantaneous direction of motion – which is significantly affected by the interactions with the neighboring cells – is introduced, the formation of swirls and collective cell detachment is strongly enhanced.

II. RESULTS AND DISCUSSION

A. Active Brownian particles with attraction

Liquid-vacuum coexistence requires strong inter-particle adhesion, so that cells can not detach from the main colony. Concurrently, the adhesion has to provide enough wiggling room that the cells remain locally mobile inside the condensed phase and provide fluidity to the colony. A long-range coordinated motion of cells, like fingering or swirls, then already emerges to some extent from the self-organized motion of cells which all vary their propulsion direction independently and diffusively. However, pronounced correlations are found to require additional alignment interactions of cell orientation and direction of motions. Here, the effect of neighbors pushing (or pulling) a cell in a certain direction is assumed to induce a reaction in the cell to reorient and align its propulsion direction with its instantaneous velocity direction.

The ABP model, where each particle is a sphere (in 3D) or a disc (in 2D) which undergoes rotational Brownian motion and additionally experiences a body-fixed driving force of constant magnitude, was developed to describe active motion on the microscale [15, 32]. This model displays a rich phase behavior, most notably motility-induced phase separation [24–26, 33], where persistence of motion and short-range repulsion induce cluster formation. Addition of a Lennard-Jones attraction leads to the formation of arrested clusters for small propulsion [28, 29, 34]. In order to obtain liquid-like properties at strong adhesion, we follow the spirit of Ref. [31] and propose an interaction potential with an extended basin of width $\bar{\sigma}$, so that

$$V_m = \begin{cases} 4\epsilon [(\sigma/r)^{12} - (\sigma/r)^6], & 0 < r \leq 2^{1/6}\sigma \\ -\epsilon, & 2^{1/6}\sigma < r \leq \tilde{r} \\ 4\epsilon [(\sigma/(r - \bar{\sigma}))^{12} - (\sigma/(r - \bar{\sigma}))^6], & \tilde{r} < r \leq r_{cut} \end{cases}$$

(see Appendix A Fig. 6). Here, σ is the particle diameter, $\tilde{r} = (2^{1/6}\sigma + \bar{\sigma})$, and ϵ is the interaction strength. This modified interaction provides a short-range repulsion or volume exclusion for the particles with separation $r < 2^{1/6}\sigma$, a force-free regime for $2^{1/6}\sigma < r \leq \tilde{r}$, and a long-range attraction for particle separation, $\tilde{r} < r < r_{cut} = 2.5\sigma$.

For activity, each ABP is subjected to a constant active force f_0 along a body-fixed propulsion direction $\hat{\mathbf{n}}_i = (\cos \theta_i, \sin \theta_i)$. The orientation θ undergoes diffusive reorientation, and may additionally experience alignment

forces. Time evolution follows a Langevin dynamics,

$$\begin{aligned} m\ddot{\mathbf{r}}_i &= -\gamma\dot{\mathbf{r}}_i + \mathbf{F}_i(\mathbf{r}_i) + f_0\hat{\mathbf{n}}_i + \sqrt{2D}\eta_i^T, \\ \dot{\theta}_i &= \sqrt{2D_r}\eta_i^R. \end{aligned} \quad (1)$$

Here, $\mathbf{F}_i = -\nabla_i V$ describes the interaction with other cells with the total potential V as a sum of all pair interactions, and $f_0 = v_0\gamma$ is the driving force which results in a self-propulsion velocity v_0 for an isolated cell experiencing a drag force due to substrate friction with drag coefficient γ , which is related to the thermal translational diffusion coefficient $D = k_B T/\gamma$ by the Einstein relation. Similarly, D_r is the rotational diffusion coefficient. The noise forces η are assumed to be Gaussian white-noise variables with $\langle \eta_i(t) \rangle = 0$ and $\langle \eta_i(t)\eta_j(t') \rangle = \delta_{ij}\delta(t-t')$. However, note that this is an active system, and thus both diffusion processes can in principle be independent active processes with different amplitudes, and thus do not need to satisfy the Einstein relation or fluctuation-dissipation theorem. In order to emphasize the importance of rotational over translational diffusion, we choose $D_r\sigma^2/D = 3$.

The cohesive nature of modeled cell colonies depends on the competition between adhesion and self-propulsion. A key parameter is the potential width $\bar{\sigma}$, which controls the fluid-like consistency of the colony. Further details about model parameters can be found in the supporting information. In the simulation results described below, all quantities are reported in dimensionless units based on thermal energy $k_B T$, particle diameter σ , and rotational diffusion time $\tau_r = 1/D_r$. We characterize the system by three dimensionless numbers, the Péclet number, $Pe = v_0\sigma^2/D = 3v_0\tau_r/\sigma$ which quantifies the activity of the system, the adhesion strength $U = \epsilon/(k_B T)$, and the potential width $\bar{\sigma}/\sigma$ which determines the wiggle room of the cells.

In order to introduce local velocity-orientation alignment, we assume alignment between propulsion direction and velocity for each cell individually [35–37]. In our simple stochastic model, Eq. 1, the orientation dynamics in this case is determined by

$$\dot{\theta}_i = \sqrt{2D_r}\eta_i^R - k_e D_r \frac{\partial}{\partial \theta} (\mathbf{n}_i \cdot \mathbf{v}_i) \quad (2)$$

Here, k_e is the strength of particle alignment. The alignment force can be interpreted as arising from a pseudo potential $V_a = -(k_e/2)(\mathbf{v} \cdot \mathbf{n})$, acting only on the orientation \mathbf{n} , but not on \mathbf{v} . Unless noted otherwise, results concern systems without velocity-alignment interactions (i.e. $k_e = 0$).

B. Liquid-Vacuum Coexistence

We begin our analysis by exploring the available phase space spanned by activity Pe and adhesive strength U . The system is initialized with a circular cell colony with

$N = 7851$ particles and a diameter 100σ (packing fraction $\phi = 0.79$) in a square simulation box of linear size 150σ . The resulting phase behavior as a function of Pe and U is displayed in Fig. 1. Here, snapshots of particle conformation after long simulation time ($t = 3300\tau_r$), together with particle mobility, measured by the mean squared displacement

$$d_m^2 = (\mathbf{r}_i(t+t') - \mathbf{r}_i(t))^2 \quad (3)$$

averaged over several reorientation times $t' = 12\tau_r$, are employed to characterize the phases. Figure 1 shows that a line $Pe \simeq U$ separates a homogeneous gas phase at $Pe > U$ from a two-phase coexistence regime for $Pe < U$. For low activity ($Pe \ll U$), the condensed phase is solid, where particles do not show any significant movement, i.e. $d_m^2 \approx 0$. As activity increases and approaches $Pe \simeq U$, cells become mobile ($d_m^2 > 1$). Finally, for large $Pe \gtrsim 100 \gg U$, attraction becomes negligible and conventional motility-induced phase separation is observed. A simple calculation, which equates the propulsion force with the maximum of the attraction force, reveals that the detachment of particle pairs occurs at $Pe = 2.4U$; for larger Pe the adhesive force is no longer strong enough to keep particles together. Note that thermal fluctuations are usually rather small in this study (because $U \gg 1$).

For $Pe \lesssim U$, cells are unable to detach from the colony, and the colony coexists with a cell vacuum outside. If $Pe \ll U$ and $U \gtrsim 8$, the system is clearly kinetically arrested, but as activity increases, the “wobble room” of the potential allows particles to break the neighbor cage and move, resulting in liquid-vacuum (L-V) coexistence. This state of a single cohesive colony is not induced by the initial conditions of a single circular patch, but also emerges from an initial random distribution of particles due to particle aggregation and cluster coarsening. To quantitatively characterize and clearly distinguish mobile cohesive colonies from the kinetically-arrested colonies, we employ the “mean squared particle separation” (MSPS). We choose random pairs of cells m and n inside the colony at time t_p , which are initially at contact with a center-center distance 1.1σ , and measure the squared separation of this pair over time. An average over N_p such pairs at different initial times t_p yields

$$MSPS(t) = \frac{1}{N_p} \sum_{N_p} (\mathbf{r}_m(t_p+t) - \mathbf{r}_n(t_p+t))^2. \quad (4)$$

A characteristic feature of the arrested dynamics in a solid phase is that particles do not exchange neighbors, so that the MSPS plateaus at $MSPS < (1.2\sigma)^2$. In a fluid phase, particles exchange neighbors at a constant rate, and MSPS increases linearly with time (see also Appendix B, Fig. 8). Thus the MSPS is good indicator of fluid-like behavior. Here, we choose $MSPS > (1.2\sigma)^2$ at time $t = 12\tau_r$ as a definition of fluid-like behavior. To quantify cohesiveness, we turn to a cluster analysis, where particles are identified to be in the same cluster if their distance is less than the cutoff distance

r_{cut} . The condensed phase-vacuum coexistence is then signaled by cluster number $N_{cl} = 1$. Figure 2(A) displays $MSPS(t = 12\tau_r)$ and N_{cl} as a function of Pe/U . For $Pe \lesssim 0.55U$, the system remains cohesive and solid. As activity increases, MSPS increases as well, but the colony remains cohesive, clearly identifying the liquid-vacuum (L-V) coexistence region. Further increasing activity ($Pe \gtrsim 0.75U$) leads to the occasional detachment of small clusters (above a threshold size) from the parent colony (see discussion below). Interestingly, occasional cluster detachment is not sufficient to disintegrate the parent colony, as detached cluster can rejoin the parent colony, which thereby coexists with a gas of small clusters.

Figure 2(B,C) display different cuts through the phase space, to elucidate the region of stability of different regimes. The results in Fig. 2(B) show that a minimum width $\bar{\sigma}/\sigma \simeq 0.1$ of the potential well is necessary to observe a liquid-vacuum coexisting phase. Thus, the width $\bar{\sigma}/\sigma$ plays a crucial role to achieve a cell colony with fluid-like dynamics at strong adhesion. The importance of Pe/U as the relevant variable to distinguish two-phase coexistence from a one-phase gas-like region, is emphasized by Fig. 2(C), which demonstrates that the boundaries between the different regimes occur at $Pe/U \simeq 0.55$, 0.75 , and 0.875 , for $U \gtrsim 20$. Note that all these boundaries appear at Pe/U values, which are much smaller than the unbinding threshold $Pe/U \simeq 2.4$ of particle pairs.

For Péclet numbers $Pe \gtrsim 0.75U$, small clusters are able to detach from the parent colony. This process can be characterized by the cluster-size distribution $P(n_{pc})$, see Fig. 2(D). The peak of the distribution for clusters in the size range from 10 to 100 indicates that particles escape collectively. We do not observe the escape of any single cell from the colony in this regime. This can be understood from a simple argument, which considers a small semi-circular patch of n_{pc} particles at the boundary of the colony (see Appendix B, Fig. 9). The patch has an interface with the colony of length proportional to $\sqrt{n_{pc}}$. If all particle orientations point in roughly the same direction (outwards), then the patch can unbind when $n_{pc} > n_{pc}^* \simeq 12.7(U/Pe)^2$, i.e. for sufficiently large patch size, a size which decreases rapidly with increasing Pe (see Appendix B for details, in particular Fig. 10). The probability for all particles in such a cluster to be roughly aligned depends on the Péclet number, as particles move toward the boundary with preferred outward orientation [38]. However, the particle mobility in the fluid phase is very small due to the dense packing of neighbors, so that the characteristic ballistic motion of ABPs for times less than τ_r is completely suppressed (see Appendix B, Fig. 7). Therefore, polar ordering is mainly seen at the edge of the colony, see Fig. 3(A). Cluster formation therefore arises mainly from the increased mobility of pre-aligned particles at the boundary.

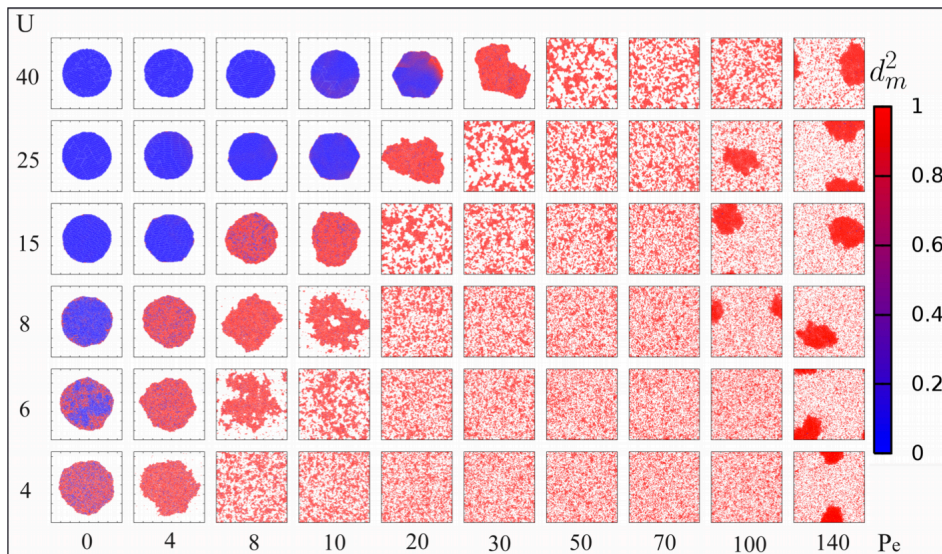


FIG. 1: Phase diagram illustrated by snapshots at the end of simulation. Here we plot the mobility profile as a function of attractive interaction U and activity Pe . We start the simulation with initial circular patch. The colour code defines the magnitude of mobility. Blue means immobile and red means highly mobile colony. ($\bar{\sigma}/\sigma = 0.3$; overall packing fraction is 0.274). See SI Movies S1 and S2 for the formation and dynamics of the cohesive colony at liquid vacuum coexistence for $U = 40$, $Pe = 30$.

C. Stress Profile - Tensile Colonies

To gain a better understanding of the properties of the liquid-like cohesive colony, we analyze the polarization field of the active force and the stress profile. Figure 3(A) shows that the averaged local polarization is zero inside the colony, but points outwards at the boundary. This is in contrast to what is typically found for motility-induced clustering [24, 26, 39–41]. The reason is that the attractive interactions keep outward-oriented particles at the boundary of the colony – which would otherwise move away – combined with the fluidity of the colony which allows local particle sorting near the boundary, similar to the behavior of isolated self-propelled particles in confinement [38, 42].

The alignment of motility forces at the boundary should lead to an increase of tensile stress. For the liquid colonies in coexistence with the vacuum phase, we find significant tensile stress in the center (see Fig. 3(C)). As expected from force balance, the stress is nearly constant inside the colony, but rapidly decreases in the boundary region where the tension is generated. The total stress in the colony has three contributions: the inter-particle force, kinetic contribution, and swim stress. At liquid-vacuum coexistence, the inter-particle contributions plays the dominant role, whereas the swim stress is comparatively small (Fig. 3(B)). Figure 4 shows the dependence of the total central stress in the colony on the activity Pe . In the solid regime, the central stress is negative due to the passive surface tension, resulting in a Laplace pressure proportional to U . Increasing activity leads to more liquid-like consistency, facilitating

enhanced outward particle orientation at the edge, and hence tensile stress. Interestingly, the stress is found to be a linearly increasing function of Pe over the whole investigated range, $0 < Pe \leq 30$, i.e. both in the solid and liquid regime of the colony. This indicates that the enhanced particle sorting occurs mainly near the edge, and an increased edge mobility exists already in the solid phase near the S-L phase boundary. A tensile stress in cell colonies is observed similarly in experiments, where the average stress within a spreading cell sheet increases as a function of distance from the leading edge [22]. In a quasi-one-dimensional (rectangular channel) geometry, the total stress in the colony is obtained by integration of the net active forces, and increases from zero outside to a finite tensile stress in the center (see Appendix B, Fig. 11).

D. Coordinated Motion – Motion Alignment

In experimental observations, long-range velocity correlations are often visible in the bulk of spreading epithelial sheets [11, 12]. ABPs with adhesion display significant velocity correlations even without explicit alignment interactions (see Appendix Fig. 13, and Refs. [15, 43]). However, as ABPs display independent orientational diffusion, it is evident that realistic long-range correlations require some type of velocity alignment. We employ a local velocity-orientation alignment mechanism, in which cell propulsion direction (=cell polarity) relaxes toward the instantaneous cell velocity, resulting from the forces induced by its neighbors [35–37], as introduced in Eq. 2.

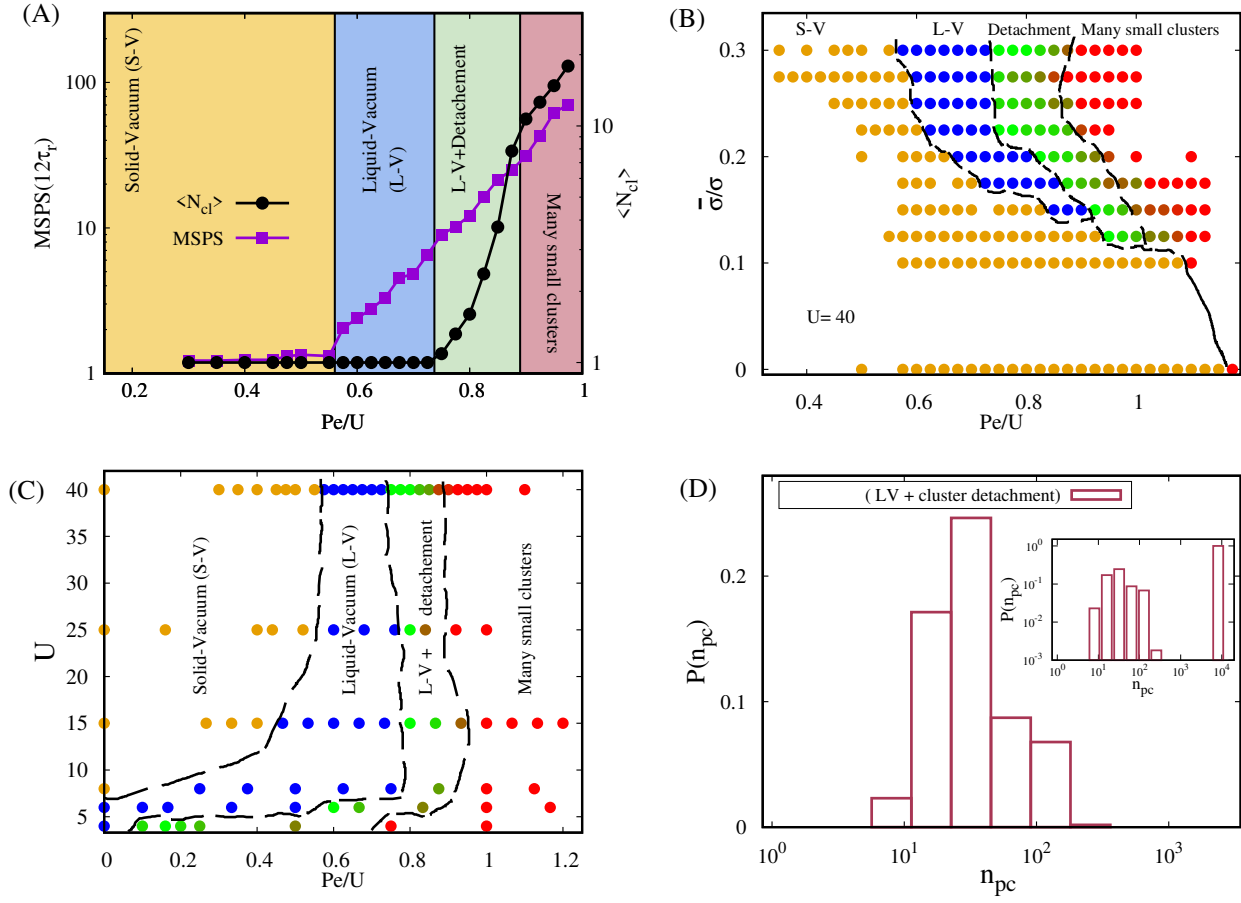


FIG. 2: (A) "MSPS" (left axis) and N_{cl} (right axis) as a function of Pe/U , for fixed $U = 40$ with increasing activity. changing Pe value. $MSPS(t)$ is calculated at time separation $t = 12\tau_r$. The orange area indicates $S - V$ coexistence, the blue area $L - V$ coexistence, the green area $L - G$ coexistence with small detached cell clusters in the gas phase, and the red area a homogeneous phase of many small clusters. Results are for $\bar{\sigma}/\sigma = 0.3$. (B) Phase diagram as a function of the potential width $\bar{\sigma}$ for fixed $U = 40$. (C) Phase diagram various U as a function of rescaled Péclet number, Pe/U , for fixed $\bar{\sigma}/\sigma = 0.3$. (D) Cluster-size distribution of detached clusters, of size n_{pc} , at $\bar{\sigma}/\sigma = 0.3$, $U = 40$, and $Pe = 32$. Inset: Same data in log-log representations, which also includes the parent colony along with the detached clusters.

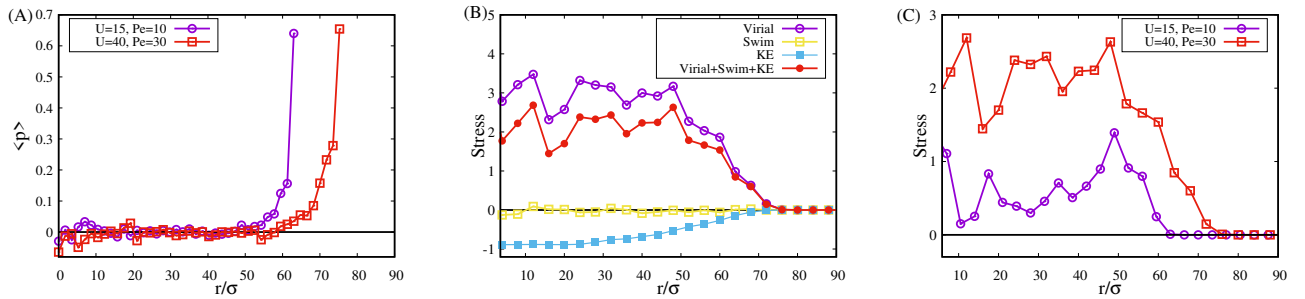


FIG. 3: (A) Averaged polarization vector of the circular patch at $\bar{\sigma} = 0.3\sigma$ at $L - V$ coexisting state for two different activity and (B) Different components of the stress at $\bar{\sigma} = 0.3\sigma$ and $U = 40$, $Pe = 30$. "Violet" represents the "virial" stress profile, yellow color represents the stress profile due to activity, "sky-blue" represents the kinetic contribution of the stress profile and "red" represents the sum of all these three contributions. (C) The total stress profile for different adhesive strength in $L - V$ coexisting states at $U = 15, 40$. The stress starts generated at the boundary region of the colony and outside of it, the stress vanishes.

Without alignment, correlations arise from a small group of cells pointing in the same direction by chance, and thus

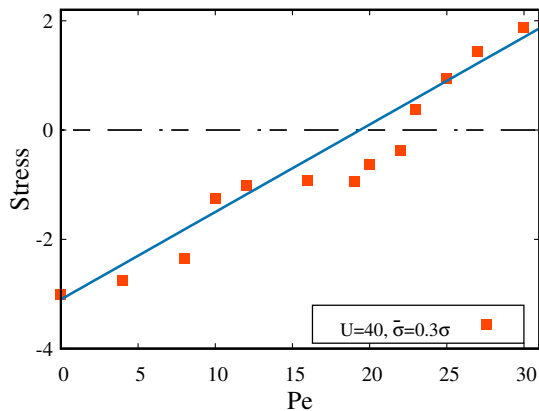


FIG. 4: Total central stress calculated in the area starting from the center to a radius 30σ as a function of activity, Pe , for $U = 40$ and $\bar{\sigma} = 0.3\sigma$. The transition from S-V to L-V coexistence occurs at $Pe = 23$ (compare Fig. 2(C)), which essentially coincides with Péclet number where central stress changes sign.

moving collectively more easily and furthermore dragging other cells along. The alignment interaction stabilizes and enhances this effect. In presence of velocity alignment, the velocity field shows an enhanced coordinated motion with prominent swirls in the bulk of the colony and fingering at the edge (see Fig. 5(A)).

We quantify the spatial correlations by the velocity-velocity correlation function

$$C_{vv}(r) = \left\langle \frac{\sum_{\mathbf{r}_i} \delta \mathbf{v}(\mathbf{r}_i) \cdot \delta \mathbf{v}(\mathbf{r}_i + \mathbf{r})}{\sum_{\mathbf{r}_i} \delta \mathbf{v}(\mathbf{r}_i) \cdot \delta \mathbf{v}(\mathbf{r}_i)} \right\rangle, \quad (5)$$

as a function of distance r , where the brackets denote an average over all directions and time. Here, velocities are measured relative to the average velocity $\bar{\mathbf{v}}$, of the whole colony, i.e. $\delta \mathbf{v}(\mathbf{r}) = \mathbf{v}(\mathbf{r}) - \bar{\mathbf{v}}$, to avoid finite-size effects. The correlations decay exponentially with a characteristic length scale, ξ_{vv} (see Appendix B, Fig. 14). Figure 5(B) displays the correlation length ξ_{vv} as a function of alignment strength k_e for various adhesive interactions. For fixed adhesion and activity, increasing alignment strength k_e facilitates a transition from the solid to the liquid state of the colony. Furthermore, the alignment coupling leads to stronger correlations, as indicated by the monotonic increase of ξ_{vv} with $k_e v_0$, and thus to swirls and fingers. Eventually, fingering is so strong that clusters detach, and the colony is no longer cohesive. However, correlation lengths up to $\xi_{vv} = 10\sigma$ can be achieved, quite comparable to the 5 to 10 times cell size obtainable in experiments [11, 15]. Also, the tensile stress at the colony center increases (see inset of Fig. 5(B)) and becomes positive at sufficiently large $k_e v_0$. The critical alignment strength $k_e v_0$, where the colony is liquefied and the tensile stress becomes positive, increases with attraction strength U .

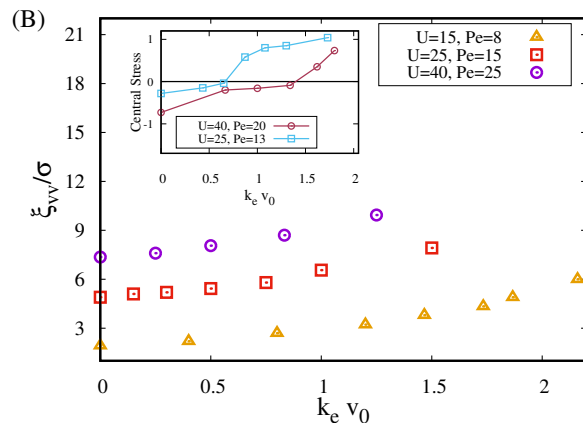
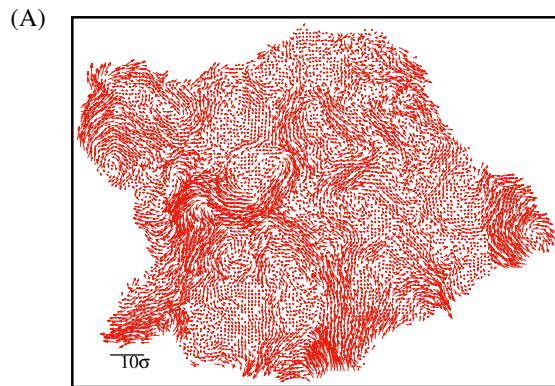


FIG. 5: Dynamics of cell colony with orientation-velocity alignment interactions. (A) Velocity fluctuation field of the full cell colony for $U = 40$, $Pe = 25$ and $k_e v_0 = 1.25$ at $\bar{\sigma} = 0.3\sigma$, which displays prominent swirls in the bulk and finger-like structures at the edge. See also Appendix B, Fig. 13. (B) Characteristic correlation length ξ_{vv} , extracted from velocity correlation, as a function of alignment strength k_e , for different attractive interactions U and activities Pe , as indicated, with $\bar{\sigma} = 0.3$. The colony is in the fluid state for $k_e v_0 = 0$. Inset: Variation of total central stress as a function of alignment strength k_e , for adhesive strength $U = 25, 40$ ($\bar{\sigma} = 0.3$). For both data sets, the colony is in the solid state for $k_e = 0$, and transits to a liquid state at $k_e v_0 \simeq 0.65$ and $k_e v_0 \simeq 1.3$ for $U = 25$ and $U = 40$, respectively.

III. CONCLUSIONS AND OUTLOOK

We have presented a minimal model for the fluidization of cell colonies, which consists of active Brownian particles with adhesion. An attractive potential with increased basin width yields non-equilibrium structures, phase behavior and dynamics, which capture relevant features of biological cell colonies. The main observation is that for moderate adhesion and propulsion, the system exhibits liquid-vacuum coexistence, i.e. all particles agglomerate into a single colony displaying liquid-like properties, while the outside remains devoid of any particles. This is reminiscent of *in vitro* experiments of MDCK colonies, where cells show strong motion, while

remaining perfectly cohesive. Furthermore, the fluidity of the colony in our model results in outward ordering of particle orientations at the edge, thus leading to tension in the colony. This is consistent with the results of traction force microscopy, which show that MDCK colonies are typically under tension [22]. Our model demonstrates that no alignment interaction or growth mechanism need to be evoked to explain such tensile forces – the motility of the cells combined with liquid properties of the colony suffice. As motility force increases, particles start to detach from the parent colony, however not as single cells but collectively in small clusters of cells. Finally, we have demonstrated how velocity-polarity alignment can further enhance fluidity, tension, and fingering of the colony, and collective cell detachment. Indeed, with velocity-polarity alignment, simulations look very reminiscent of real MDCK colonies, displaying strong fingering at the edge, high tension and long-ranged velocity correlations.

Our model also provides a tentative explanation for another biological phenomenon. When metastatic cells detach from a tumor, they typically detach collectively, as small groups of five cells or large aggregates [44–46], into the stroma and migrate to reach blood or lymph vessels. At the edge of the liquid-vapor region of our model, particles show exactly this type of behavior; the colony is no longer perfectly cohesive, but clusters of cells begin to detach.

An interesting next question is how these results will be affected by cell growth. Of course, if growth is slow, the dynamics will be independent of growth and the phenomenology will be unchanged. However, when time scales of growth and motion become comparable, novel phenomena may arise.

Acknowledgments

Financial support by the Deutsche Forschungsgemeinschaft (DFG) through the priority program SPP1726 “Microswimmers – from single particle motion to collective behavior” is gratefully acknowledged. The authors also gratefully acknowledge the computing time granted through JARA-HPC on the supercomputer JU-RECA [47] at Forschungszentrum Jülich.

Appendix A: Attractive Brownian Particles: Model and Analysis of Simulation Data

1. Simulation parameters

For numerical implementation of our model, we use the LAMMPS molecular simulation package, with in-house modifications to describe the angle potential and the propulsion forces, as described in the main text. The system consists of $N = 7851$ particles (cells) in a 2D square simulation box of size $L_x = L_y = 150\sigma$ with periodic boundary conditions, unless noted otherwise.

With velocity-orientation-alignment interaction, the simulation is carried out in a box of size $L_x = L_y = 250\sigma$. For the extended LJ interaction potential, see Fig. 6, we use the cut-off distance $r_{cut} = 2.5\sigma$. For numerical efficiency, we chose a finite mass $m = 1$ and drag coefficient $\gamma = 100$ such that the velocity relaxation time m/γ is much smaller than all physical time scales. The equations of motion are integrated with a velocity Verlet algorithm, with time step $\Delta t = 0.001$. Each simulation is run for at least 11×10^7 time steps, with rotational diffusion coefficient $D_r = 0.03$ this corresponds to a total simulation time longer than $3000\tau_r$, where τ_r is the rotational decorrelation time.

2. Polarization Vector

We define the spatial-temporal average polarization p for the quasi-circular cell colony by the projection of the orientation vector $\hat{\mathbf{n}}$ of the particle on the radial direction from the center of mass of the colony, i.e.,

$$\langle p(r', t) \rangle = \frac{1}{N} \sum_{i=1}^N (\hat{\mathbf{n}}_i \cdot \hat{\mathbf{r}}'_i) \delta(r' - |\mathbf{r}'_i|) / \sum_{i=1}^N \delta(r' - |\mathbf{r}'_i|) \quad (\text{A1})$$

where $\mathbf{r}'_i = \mathbf{r}_i - \mathbf{r}_{cm}$, and \mathbf{r}_{cm} is the center-of-mass position at a particular time t . Here, $\delta(r)$ is a smeared-out δ -function of width σ . $\langle p \rangle$ is further averaged over time.

3. Stress calculation

In ABP systems with short-range repulsion, it has been shown that the pressure is a state function, depending only on activity, particle density, and interaction potential, but *not* on the interaction with confining walls [41, 48–50]. In comparison to passive systems, activity implies a new contribution to pressure, which is called the swim pressure. The calculation of the local stress in an ABP system is a matter of an ongoing debate, which mainly concerns the form of the active term. We follow Ref. [41], and define the stress in a volume ΔV by

$$\Delta V \Sigma_{\alpha\alpha} = \sum_{i=1}^N m \langle \dot{\mathbf{r}}_i^2 \Lambda_i \rangle - \frac{\gamma}{\gamma_R} \sum_{i=1}^N \langle v_0 \mathbf{n}_i \cdot \dot{\mathbf{r}}_i \Lambda_i \rangle + \frac{1}{2} \sum_{i=1}^N \sum_{j=1}^N \langle \lambda_{ij} \mathbf{r}_{ij} \cdot \mathbf{F}_{ij} \rangle \quad (\text{A2})$$

where $\dot{\mathbf{r}}_i$, \mathbf{F}_i ($i = 1, \dots, N$) denote the velocity and force of particle i , respectively. \mathbf{F}_{ij} represents the pair wise interaction between particle i and j and $\mathbf{r}_{ij} = \mathbf{r}_i - \mathbf{r}_j$. Here $\Sigma_{\alpha\alpha}$ are the diagonal stress-tensor components. γ_R is the damping factor which is related to the rotational diffusion coefficient as $\gamma_R = 2D_r$. Λ_i determines the volume ΔV , where $\Lambda_i(\mathbf{r})$ is unity when particle i is within ΔV and zero otherwise. λ_{ij} denotes the fraction of the

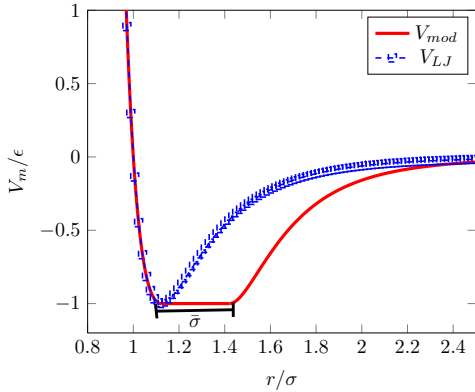


FIG. 6: Modified Lennard-Jones (LJ) potential (red colored curve) is modified by inserting a plateau of width $\bar{\sigma}$ at the minimum of this potential. The usual LJ potential is shown by blue crosses.

line connecting particle i and j inside of the volume ΔV . The first and the last term in (A2) are the classic kinetic contribution and the contribution of inter-particle interactions. The second term denotes the active-force contribution in the stress calculation. Notably, in the fluid-vacuum state we are focusing on in this work, the active stress component is negligible compared to the inter-particle interaction contribution. This is in line with results for the pressure contributions in repulsive ABP systems at coexistence between a high-density and a low-density phase, where the swim pressure in the high-density phase is negligible [41].

Appendix B: Supporting Considerations and Results

1. Particle Mobility in Vacuum, Gas, and Fluid Phases

A single, isolated ABP has a characteristic mean square displacement, with ballistic motion ($\text{MSD} \sim v_0^2 t^2$) at short times $t < \tau_r$, and a diffusive motion ($\text{MSD} \sim v_0^2 \tau_r t$) for $t > \tau_r$ [51]. This is the behavior we observe in the vacuum phase, see Fig. 7. A very similar behavior is found in the gas phase, at packing fraction $\phi = 0.274$, but now the particle velocity is significantly reduced due to frequent collisions with other particles, while the crossover time τ_r remains unaffected. However, the behavior changes drastically in the fluid-like phase, where the collisions and attractive interactions completely suppress the ballistic regime, see Fig. 7.

A very similar dynamic behavior is observed in the mean squared particle separation (MSPS), see Fig. 8. The time dependence in the fluid phase is dominated by linear diffusion behavior, while in the solid (jammed) phase it is strongly sublinear.

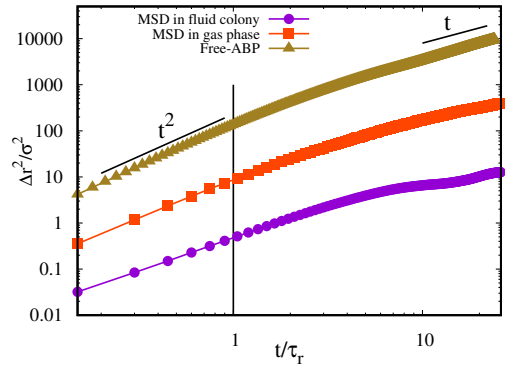


FIG. 7: Mean square displacement (MSD) in three different states: (i) In the bulk of "fluid-like" colony (purple circles) with $U = 40$ and $Pe = 30$, (ii) in the "gas" phase ($U = 40$ and $Pe = 41$ and packing fraction $\phi = 0.274$), and (iii) in the "vacuum" phase (brown triangles) with $Pe = 41$.

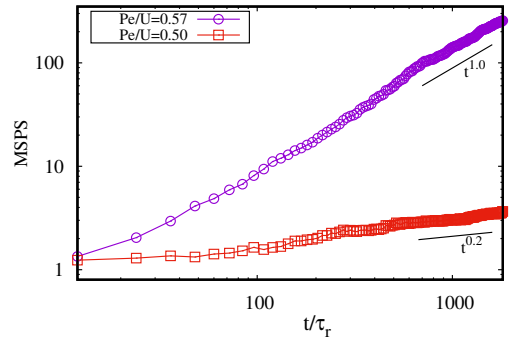


FIG. 8: Mean squared particle separation ($MSPS$) as a function of time for two different Pe numbers at $U = 40$ and $\bar{\sigma} = 0.3$. At $Pe/U = 0.5$, $MSPS$ remains constant at short times, indicative of no neighbor exchange, and shows subdiffusive behavior at longer time. However, at $Pe/U = 0.57$, the time evolution of $MSPS$ shows a long-time linear behavior, indicative of constant neighbor exchange and liquid-like behavior.

2. Minimum Cluster Size for Detachment

For our model system, particles can only escape from the parent colony in the form of a small cluster at larger adhesive strength ($U \geq 10$). Let us consider the following simplified model. A semi-circular cluster of particles has formed at the colony edge, where all particle orientations are aligned and are pointing outwards normal to the interface. In this idealized situation, we can address the question about the number of particles in the cluster, and the Pe number required to separate the cluster against the adhesive force from the parent colony.

Let n_{pc} be the number of particles in the cluster. For packing in a roughly triangular lattice with lattice constant $a = \sigma + \bar{\sigma}/2$, this implies a cluster radius

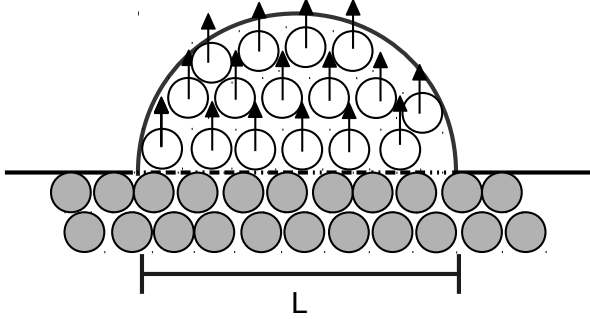


FIG. 9: A semi-circular cluster of particles formed at the colony edge. All particles in this region are assumed to be aligned and to be oriented in the outward direction, normal to the interface, as indicated by the arrows. The length of the interface between parent colony and detaching cluster is L .

$R_{cl}/a = (\sqrt{3}/\pi)^{1/2} n_{pc}^{1/2}$. The length of the interface between cluster and parent colony is $L = 2R$, see Fig. 9. Along the interface, there are L/a bonds between particles on both sides of the interface, which generate the same maximum force as for the detachment of a single particle, where bond breakage occurs at $Pe/U = 2.4$ (see main text). Thus, we have the force balance for the cluster break-off, $n_{pc}Pe = 2.4(L/a)U = 4.8(\sqrt{3}/\pi)^{1/2}Un_{pc}^{1/2}$, which implies

$$n_{pc,min} = \frac{\sqrt{3}}{\pi} \left(\frac{4.8U}{Pe} \right)^2. \quad (\text{B1})$$

Hence, with increasing activity Pe at constant adhesive strength U , the minimal size of detached clusters is expected to decrease rapidly. Figure 10 shows simulation results for the number of particles present in the smallest cluster $n_{pc,min}$ as a function of Pe/U . This demonstrates that beyond the liquid-vacuum region, n_{pc} rapidly decreases with increasing activity Pe and eventually reaches a "gas-like" phase, where single-particle detachment from the parent colony, i.e. $n_{pc,min} = 1$, is observed.

Furthermore, we can use Eq. (B1) to estimate the cluster size when cluster break-off first becomes possible, at $Pe/U \simeq 0.75$, which is about $n_{pc} \simeq 20$, in reasonable agreement with the lower cutoff of the cluster-size distribution in Fig. 2(D) of the main text.

3. Probability Distributions of Aligned Particle Clusters at Colony Edge

For randomly oriented particles, the probability to find a cluster in which the orientations of all particles have a positive projection into one chosen direction is $2^{-N_{cl}}$, which is very small for clusters of size 10 or larger. However, there is a sorting mechanism which strongly en-

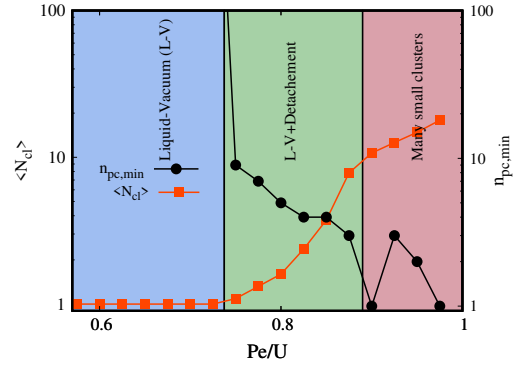


FIG. 10: Average cluster size $\langle N_{cl} \rangle$ (left axis) and size of smallest cluster $n_{pc,min}$ (right axis) as a function of Pe/U , for fixed $U = 40$ with increasing activity ($\bar{\sigma}/\sigma = 0.3$). The blue area indicates $L - V$ coexistence, the green area $L - V$ coexistence with small detached clusters in the gas phase, and the red area a homogeneous phase of many small clusters.

hances this probability, which is the active motion of particles toward the colony edge, where they arrive with roughly the right orientation [38]. However, due to the diffusive motion in the bulk of the colony, see Fig. 7, this mechanism can only operate very close to the colony edge. The polarization profile (Fig. 3(A) of the main text) shows a high polarization of $p = 0.65$ at the boundary. Thus, properly oriented particles only have to diffuse laterally along the boundary to form clusters for detachment. This mechanism is supported by simulations, which allow the tracking of the history of cluster development.

4. Stress Calculation in a Quasi-One-Dimensional Geometry

As a further test to our stress estimates, we use force balance to obtain an independent measure of stress, similar to traction-force microscopy setups [22]. Under the physical interpretation of our system that the particles are cells which exert an active force γv_0 on the substrate in order to move against friction forces $-\gamma v$, the traction force of each particle is $T = \gamma v_0 \hat{\mathbf{n}} - \gamma \mathbf{v}$. In one dimension, force balance is closed, and we can calculate a change of stress via force balance. We simulate a quasi-one-dimensional geometry with a nearly flat interface. The system consists of a 2D channel of dimensions $L_x = 6 * L_y$ and $L_y = 20\sigma$, filled with $N = 1200$ particles arranged initially to fill half the channel. This system is subjected to periodic boundary conditions in both x and y directions. The stress within the cell colony is calculated via integration of force balance (assuming zero stress outside the colony).

With the parameters $\bar{\sigma} = 0.3\sigma$, adhesive strength $U = 15$ and activity $Pe = 13$, the cell colony is in liquid-vacuum coexistence, see Fig. 11(top). The stress pro-

file in the direction (x) normal to the interface is shown in Fig. 11(bottom), while the tangential stress vanishes. Figure 11 also shows that the estimations of the stress profile calculated from the traction forces and from the virial expression agree quite well.

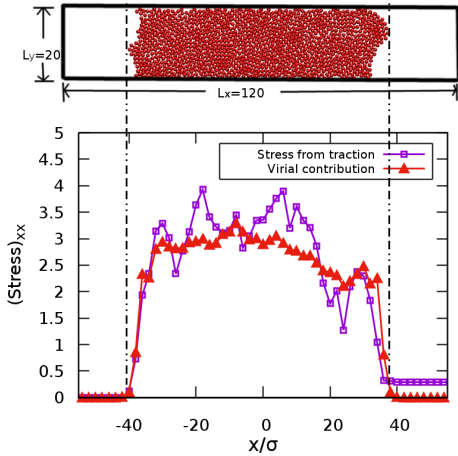


FIG. 11: Top: Snapshot from the simulation in a quasi-one-dimensional rectangular channel, for a cell colony in liquid-vacuum coexistence. The parameters are $\bar{\sigma} = 0.3\sigma$, adhesive strength $U = 15$ and activity $Pe = 13$. Bottom: Stress calculated from traction forces and virial contribution.

5. Origin of Tension in Attractive ABP Clusters – a Toy Model

Why are colonies of attractive ABPs under tension, while cluster of repulsive ABPs in the state of motility-induced phase separation are under pressure? A simple toy model can elucidate the underlying mechanism. Consider two ABPs which are connected by a harmonic bond [52]. This bond represents the interaction between an ABP at the colony edge, and one (or more) ABP further inside the bulk. In case of a sufficiently high Péclet number (large propulsion, slow rotational diffusion), the dumbbell quickly reaches a quasi-stationary, torque-free state, see Fig. 12(A,B). In this state, the force can be separated into a propelling component with direction $(\mathbf{n}_1 + \mathbf{n}_2)$, normal to the instantaneous bond vector $\mathbf{r} \sim (\mathbf{n}_1 - \mathbf{n}_2)$, and a bond stretching component, see Fig. 12(B,C). The stretching force is

$$\begin{aligned} f_{ext} &= f_0 |\mathbf{n}_1 \cdot \hat{\mathbf{r}}| = f_0 |\cos(\theta_1)| \\ &= f_0 \sqrt{(1 - \mathbf{n}_1 \cdot \mathbf{n}_2)/2} \\ &= |\sin((\varphi_1 - \varphi_2)/2)| \end{aligned} \quad (\text{B2})$$

where φ_i is the orientation angle of \mathbf{n}_i with respect to some fixed axis. This stretching force has to be averaged over all orientations \mathbf{n}_1 and \mathbf{n}_2 , which yields

$$\langle f_{ext} \rangle = \frac{2}{\pi} f_0 \quad (\text{B3})$$

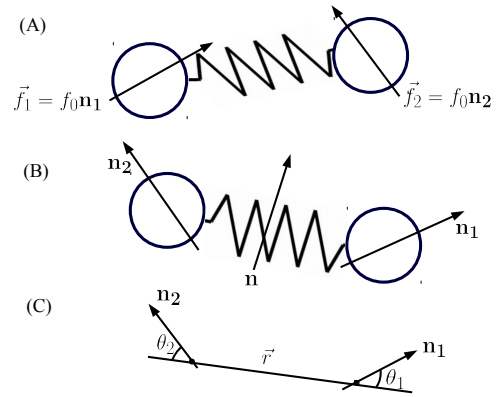


FIG. 12: Arrangement and forces of ABP dumbbells. (A) Two connected ABPs with randomly oriented propulsion forces \mathbf{f}_1 and \mathbf{f}_2 . (B) A short time t later, with $\sigma/v_0 < t < \tau_r$, the ABP orientations remain essentially unchanged, but the particles have rearranged to form a quasi-stationary, torque-free state, in which the bond is under tension. The dumbbell also moves in direction $\mathbf{n} = \mathbf{n}_1 + \mathbf{n}_2$ normal to the bond vector \mathbf{r} . (C) In the quasi-stationary state, the ABP orientation vectors form angles θ_1 and θ_2 with the bond vector $\mathbf{r} \sim (\mathbf{n}_1 - \mathbf{n}_2)$, with $\theta_1 = \theta_2$.

Stress $\Sigma_{\alpha\alpha}$ is force per length, i.e. $\Sigma_{\alpha\alpha} \simeq \langle f_{ext} \rangle / a \simeq \langle f_{ext} \rangle / \sigma$. We can thus use Eq. B3 to estimate the tensile stress as a function of Péclet number. With $f_0 = \gamma v_0$, $D = k_B T / \gamma$, $D_r = 3D / \sigma^2$, and $Pe = 3v_0 / (\sigma D_r)$, we obtain $f_0 = Pe$ (in our dimensionless units). Thus, we predict $\Sigma = \Sigma_0 + (2/\pi)Pe$ from our toy-model calculation. The linear dependence agrees well with the simulation results for the cell colony, see Fig. 4 of main text. However, the slope estimated from Fig. 4 is 0.16, about a factor 4 smaller than the toy-model prediction. Two obvious reasons for this overestimation of the slope in the toy model are that (i) the bond vector takes all orientations with equal probability, but only orientations roughly perpendicular to the interface contribute to the stress (factor 2), and (ii) the hard-core repulsion between ABPs is neglected, which sometimes leads to a pressure (negative tension) (maybe another factor 2) – so that the overall agreement is quite satisfactory.

6. Velocity Correlation Function

To quantify collective cell migration, we map out the velocity field. Snapshots of the simulations in Fig. 13 demonstrate that particles display strongly coordinated motion. To further quantify the correlations, we calculate the velocity correlation function C_{vv} as described in Eq. 5 of the main text. Figure 14 shows $C_{vv}(r)$. On short length scales, the velocity correlations decay exponentially with a characteristic length scale ξ_{vv} . We estimate ξ_{vv} by fitting the simulation data by $\exp(-r/\xi_{vv})$. The dependence of the ξ_{vv} on U and Pe is discussed in the main text, see Fig. 5(B).

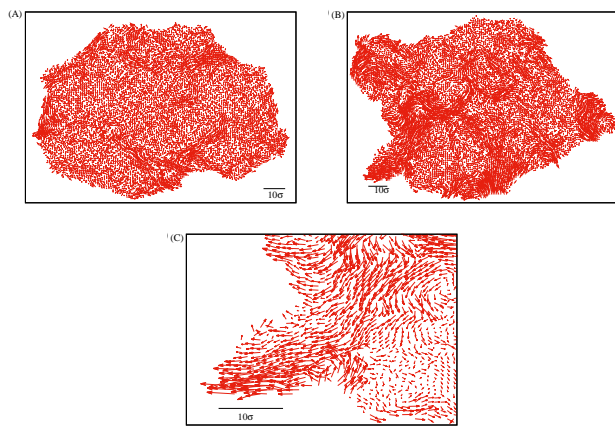


FIG. 13: (Top) Velocity field (left) without and (right) with explicit alignment interaction at $U = 40$, $Pe = 25$, $\bar{\sigma} = 0.3$, and $k_e v_0 = 1.25$. (Bottom) Velocity field in the finger-like structure of the fluid-like in presence of alignment interaction ($k_e v_0 = 1.25$).

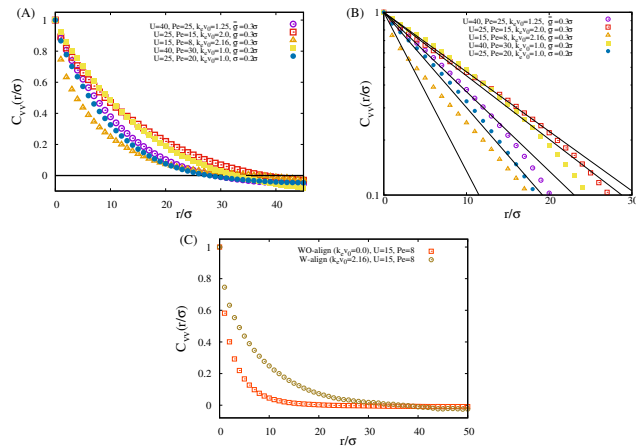


FIG. 14: Velocity correlation function $C_{VV}(r/\sigma)$ for a system with velocity-alignment interaction in the L-V region. (A) Spatial dependence for various attraction strengths U , Péclet numbers Pe , and alignment interaction strengths $k_e v_0$, and widths $\bar{\sigma}$ of the attraction well, as indicated. (B) Same data as in (A), with exponential decay demonstrated by log-lin representation. (C) Comparison of correlation functions with (w-align) and without velocity alignment (wo-align).

Figure 14 shows C_{vv} with and without alignment interaction. Velocity-alignment interactions strengthen correlated motion and result in more swirl-like patterns, as indicated by a small negative minimum in C_{vv} .

-
- [1] P. Martin and S. M. Parkhurst, *Development* **131**, 3021 (2004).
 - [2] P. Friedl, Y. Hegerfeldt, and M. Tusch, *Int. J. Dev. Biol.* **48**, 441 (2004).
 - [3] V. Lecaudey and D. Gilmour, *Curr. Opin. Cell. Biol.* **18**, 102 (2006).
 - [4] K. Burridge and M. Chrzanowska-Wodnicka, *Annu. Rev. Cell Dev. Biol.* **12**, 463 (1996).
 - [5] G. Giannone, B. J. D. Thaler, O. Rossier, Y. Cai, O. Chaga, G. Jiang, W. Beaver, H. Döbereiner, Y. Freund, G. Borisy, and M. P. Sheetz, *Cell* **128**, 561 (2007).
 - [6] D. A. Lauffenburger and A. F. Horwitz, *Cell* **84**, 359 (1996).
 - [7] K. Keren, Z. Pincus, G. M. Allen, E. L. Barnhart, G. Marriott, A. Mogilner, and J. A. Theriot, *Nature* **453**, 475 (2008).
 - [8] Y. Matsubayashi, M. Ebisuya, S. Honjoh, and E. Nishida, *Curr. Biol.* **14**, 731 (2004).
 - [9] A. Puliafito, L. Hufnagel, P. Neveu, S. Streichan, A. Sigal, D. K. Fygenson, and B. I. Shraiman, *Proc. Natl. Acad. Sci. U.S.A.* **109**, 739 (2012).
 - [10] M. Bindschadler and J. L. McGrath, *J. Cell Sci.* **120**, 876

- (2007).
- [11] T. E. Angelini, E. Hannezo, X. Trepát, M. Marquez, J. J. Fredberg, and D. A. Weitz, *Phys. Rev. Lett.* **104**, 168104 (2010).
- [12] T. E. Angelini, E. Hannezo, X. Trepát, M. Marquez, J. J. Fredberg, and D. A. Weitz, *Proc. Natl. Acad. Sci. U.S.A.* **108**, 4714 (2011).
- [13] D. Bi, J. H. Lopez, J. M. Schwarz, and M. L. Manning, *Nat. Phys.* **11**, 1074 (2015).
- [14] D. Bi, X. Yang, M. C. Marchetti, and M. L. Manning, *Phys. Rev. X* **6**, 021011 (2016).
- [15] S. Garcia, E. Hannezo, J. Elgeti, J. F. Joanny, P. Silberzan, and N. S. Gov, *Proc. Natl. Acad. Sci. U.S.A.* **112**, 15314 (2015).
- [16] M. Krajnc, S. Dasgupta, P. Zihlerl, and J. Prost, *Phys. Rev. E* **98**, 022409 (2018).
- [17] T. Omelchenko, J. M. Vasiliev, I. M. Gelfand, H. H. Feder, and E. M. Bonder, *Proc. Natl. Acad. Sci. U.S.A.* **100**, 10788 (2003).
- [18] M. Poujade, E. G. Mongrain, A. Hertzog, J. Jouanneau, P. Chavrier, B. Ladoux, A. Buguin, and P. Silberzan, *Proc. Natl. Acad. Sci. U.S.A.* **104**, 15988 (2007).
- [19] T. E. Angelini, E. Hannezo, X. Trepát, M. Marquez, J. J. Fredberg, and D. A. Weitz, *Biophys. J.* **98**, 1790 (2010).
- [20] M. Vishwakarma, J. D. Russo, D. Probst, U. S. Schwarz, T. Das, and J. P. Spatz, *Nat. Commun.* **9**, 3469 (2018).
- [21] We use the term 'vacuum' here somewhat loosely to represent a phase of extremely low cell density.
- [22] X. Trepát, M. R. Wasserman, T. E. Angelini, E. Millet, D. A. Weitz, J. P. Butler, and J. J. Fredberg, *Nat. Phys.* **5**, 426 (2009).
- [23] M. Reffay, M. C. Parrini, O. Cochet-Escartin, B. Ladoux, A. Buguin, S. Coscoy, F. Amblard, J. Camonis, and P. Silberzan, *Nat. Cell Biol.* **16**, 217 (2014).
- [24] Y. Fily and M. C. Marchetti, *Phys. Rev. Lett.* **108**, 235702 (2012).
- [25] G. S. Redner, M. F. Hagan, and A. Baskaran, *Phys. Rev. Lett.* **110**, 055701 (2013).
- [26] A. Wysocki, R. G. Winkler, and G. Gompper, *EPL* **105**, 48004 (2014).
- [27] J. Elgeti, R. G. Winkler, and G. Gompper, *Rep. Prog. Phys.* **78**, 056601 (2015).
- [28] G. S. Redner, M. F. Hagan, and A. Baskaran, *Phys. Rev. E* **88**, 012305 (2013).
- [29] R. M. Navarro and S. M. Fielding, *Soft Matter* **11**, 7525 (2015).
- [30] V. Prymidis, S. Paliwal, M. Dijkstra, and L. Filion, *J. Chem. Phys.* **145**, 124904 (2016).
- [31] I. R. Cooke, K. Kremer, and M. Deserno, *Phys. Rev. E* **72**, 011506 (2005).
- [32] B. Smeets, R. Alert, J. Pešek, I. Pagonabarraga, H. Ramon, and R. Vincent, *Proc. Natl. Acad. Sci. U.S.A.* **113**, 14621 (2016).
- [33] I. Buttinoni, J. Bialké, F. Kümmel, H. Löwen, C. Bechinger, and T. Speck, *Phys. Rev. Lett.* **110**, 238301 (2013).
- [34] B. M. Mognetti, A. Sarić, S. Angioletti-Uberti, A. Cacciuto, C. Valeriani, and D. Frenkel, *Phys. Rev. Lett.* **111**, 245702 (2013).
- [35] B. Szabó, G. J. Szöllösi, B. Gönci, Z. Jurányi, D. Selmeczi, and T. Vicsek, *Phys. Rev. E* **74**, 061908 (2006).
- [36] M. Basan, J. Elgeti, E. Hannezo, W. J. Rappel, and H. Levine, *Proc. Natl. Acad. Sci. U.S.A.* **110**, 2452 (2013).
- [37] K. N. T. Lam, M. Schindler, and O. Dauchot, *New J. Phys.* **17**, 113056 (2015).
- [38] J. Elgeti and G. Gompper, *EPL* **101**, 48003 (2013).
- [39] Y. Fily, S. Henkes, and M. C. Marchetti, *Soft Matter* **10**, 2132 (2014).
- [40] P. Digregorio, D. Levis, A. Suma, L. F. Cugliandolo, G. Gonnella, and I. Pagonabarraga, *Phys. Rev. Lett.* **121**, 098003 (2018).
- [41] S. Das, G. Gompper, and R. G. Winkler, *Sci. Rep.* **9**, 6608 (2019).
- [42] Y. Fily, A. Baskaran, and M. F. Hagan, *Soft Matter* **10**, 5609 (2014).
- [43] N. Sepúlveda, L. Petitjean, O. Cochet, E. Grasland-Mongrain, P. Silberzan, and V. Hakim, *PLOS Comput. Biol.* **9**, e1002944 (2013).
- [44] P. Friedl and D. Gilmour, *Nat. Rev. Mol. Cell Biol.* **10**, 445 (2009).
- [45] J. J. Christiansen and A. K. Rajasekaran, *Cancer Res.* **66**, 8319 (2006).
- [46] A. G. Clark and D. M. Vignjevic, *Curr. Opin. Cell Biol.* **36**, 13 (2015).
- [47] Jülich Supercomputing Centre, *J. Large-Scale Res. Facil.* **4**, A132 (2018).
- [48] S. C. Takatori, W. Yan, and J. F. Brady, *Phys. Rev. Lett.* **113**, 028103 (2014).
- [49] A. P. Solon, Y. Fily, A. Baskaran, M. E. Cates, Y. Kafri, M. Kardar, and J. Tailleur, *Nat. Phys.* **11**, 673 (2015).
- [50] T. Speck and R. L. Jack, *Phys. Rev. E* **93**, 062605 (2016).
- [51] J. R. Howse, R. A. L. Jones, A. J. Ryan, T. Gough, R. Vafabakhsh, and R. Golestanian, *Phys. Rev. Lett.* **99**, 048102 (2007).
- [52] R. G. Winkler, *Soft Matter* **12**, 3737 (2016).